Available online at www.sciencedirect.com
ScienceDirect
Trans. Nonferrous Met. Soc. China 34(2024) 2889−2899
Transactions of Nonferrous Metals Society of China
www.tnmsc.cn

Microstructure and ablation behavior of Zr-based ultra-high-temperature gradient composites

Qing-hua LIU[1], Tian TIAN[1], Wei SUN[1,2], Hong-bo ZHANG[1], Xiang XIONG[1]

1. State Key Laboratory of Powder Metallurgy, Central South University, Changsha 410083, China;
2. National Key Laboratory of Science and Technology on High-strength Structural Materials, Central South University, Changsha 410083, China

Received 25 March 2023; accepted 16 January 2024

Abstract: To obtain high-performance Zr-based ultra-high-temperature composites, Zr-based ultra-high-temperature gradient composites were prepared by changing the laying method of the infiltrant via reactive melt infiltration. The effects of different infiltrant laying methods on the microstructure and ablative properties of Zr-based ultrahigh-temperature gradient composites were investigated. The results showed that the gradient structure of the Zr-based ultrahigh-temperature gradient composites differed when the composition ratio of the infiltrant was changed. When the thicknesses of the Zr/Mo/Si layers were 6/4/12 mm and 8/2/12 mm, the SiMoZrC solid solution content in the samples increased and decreased along the infiltration direction, respectively. The gradient samples were ablated in an oxyacetylene flame at 3000 °C for 40 s. The ablation resistance of the sample was the highest when the infiltrant was a powder and the thickness of the Zr/Mo/Si layer was 6/4/12 mm.

Key words: reactive melt infiltration; ceramic-matrix composites; gradient material; microstructure; ablation property

1 Introduction

Carbon/carbon (C/C) composites are considered promising materials for high-temperature aerospace structural materials and thermal protection systems owing to their low density and thermal expansion coefficient [1]. However, they easily react with oxygen at 400 °C in an oxidizing atmosphere, which tends to degrade the properties of the materials. This limits the application under extreme conditions. To solve this problem, researchers have used ultra-high-temperature ceramics, such as ZrC, HfC, TaC, and SiC, to modify the C/C composites.

Both ZrC and its oxidation product ZrO_2 have good thermal stability and high melting point (3420 and 2677 °C, respectively). Thus, C/C composites modified with ultra-high-temperature ceramics have the greatest potential as materials for use in modification technologies [2,3]. Numerous investigations on C/C−ZrC composites have shown that the addition of SiC ceramics effectively improves the ablation resistance. This is because the oxidized SiO_2 glass can effectively fill the pores and cracks in the ZrO_2 layer [4−9]. However, an SiO_2 depletion layer appears during the oxidation of C/C−ZrC−SiC. To solve this problem, some researchers have improved the ablation resistance by adding high-boiling-point oxides [10−12], whereas others have added $MoSi_2$ to provide additional Si sources that can reduce the appearance of the SiO_2 depletion layer [13−15]. Experiments have shown that the C/C composites modified by a Zr−Mo−Si system exhibit good ablation resistance [16].

The mismatch of thermal expansion coefficient

Corresponding author: Wei SUN, Tel: +86-13808478540, E-mail: sunweimse@csu.edu.cn
DOI: 10.1016/S1003-6326(24)66583-0

is a challenge for ultra-high-temperature ceramic modified C/C composites. Gradient materials with excellent development prospects in the aerospace field can effectively resolve the mismatch between the thermal expansion coefficients of ultra-high-temperature ceramics and carbon fibers. The preparation methods for gradient ultra-high-temperature composites include plasma spraying, in situ reaction, chemical vapor deposition, and reactive melt infiltration. Plasma spraying can easily control the gradient composition; however, the gradient coating has holes and cracks, and the ceramic powder may not melt [17−19]. The in situ reaction process is complicated, cracks are easily produced [20,21], and chemical vapor deposition has a long preparation period [22]. However, the reaction infiltration method can be used to prepare materials with compact structures and excellent ablation resistance within a short preparation period and at a low cost [23].

In this study, gradient Zr-based ultra-high-temperature composites were prepared via reactive infiltration, providing a new method for preparation of gradient ultra-high-temperature materials with excellent performance and dense structures. The melt formation process was affected by altering the laying method of infiltrant. Accordingly, gradient Zr-based ultra-high-temperature composites were prepared. The microstructure, melt-infiltration mechanism, and ablation properties of the Zr-based ultra-high-temperature gradient composites were investigated. The ablation properties of the Zr-based ultra-high-temperature gradient composites were examined to investigate the ablation behavior and ablation mechanism of the materials.

2 Experimental

2.1 Materials

The raw materials mainly included C/C composites (T700, PAN-based carbon fiber, Japan) and Zr (d~50 μm, 99.99% purity, Beijing Xing Rong Yuan Technology Co., Ltd., China), Mo (d1−3 μm, 99.9% purity, Qinhuangdao Yinuo High-tech Material Development Co., Ltd., China), and Si powders (d~75 μm, Changsha Tijo Metal Material Co., Ltd., China). First, the C/C composites were placed in a graphite crucible. The Zr, Mo and Si powders that were subjected to different treatment methods, were placed on the C/C composites at the specific heights in the order (from top to bottom) of the Zr, Mo, Si and C/C preforms. Table 1 lists the thickness of Zr, Mo and Si layers and the density of C/C composites before infiltration. All the samples were heated to 2000 °C, kept for 3 h, and finally cooled to room temperature. The infiltrant consisted of Zr, Mo and Si powders, and the raw materials were treated using two methods. The first involved laying the powders in the order of Zr, Mo and Si directly on the C/C composites, and the second involved using the prepared tablets. The Zr, Mo and Si powders were separately mixed with paraffin wax (2 wt.%) and pressed onto tablets of mold size of 65 mm × 25 mm. Finally, the Zr, Mo and Si briquettes were placed in a graphite crucible, heated to 1400 °C, and kept for 1 h.

2.2 Ablation test

Ablation tests were performed on the Zr-based ultra-high-temperature composites using an oxyacetylene torch. The pressures and fluxes of oxygen and acetylene were 0.4 MPa and 1.960 L/s, 0.095 MPa and 0.696 L/s, respectively. The oxyacetylene flame temperature was 3000 °C, ablation time was 40 s, and distance between the gun tip and ablated surface was 21 mm. The linear and mass ablation rates of the samples were calculated using Eqs. (1) and (2), respectively:

$$R_l=(l_0-l_1)/t \quad (1)$$

$$R_m=(m_0-m_1)/t \quad (2)$$

where R_l is the linear ablation rate; l_0 and l_1 are the

Table 1 Thickness of Zr, Mo and Si layers and density of C/C composites before infiltration

Sample	Density of porous C/C/(g·cm^{-3})	Infiltrant	Thickness of Si/mm	Thickness of Mo/mm	Thickness of Zr/mm
P6	1.36	Powder	12	4	6
P8	1.37	Powder	12	2	8
P10	1.14	Powder	12	0	10
PT6	1.35	Prepared tablet	12	4	6

thickness of the ablation center before and after ablation, respectively; R_m is the mass ablation rate; m_0 and m_1 are the mass of the material before and after ablation, respectively; t is the ablation time of the material in oxyacetylene.

2.3 Characterization

The morphologies of the Zr-based ultra-high-temperature composites were analyzed using a scanning electron microscope (SEM) equipped with an energy dispersive spectrometer (EDS). The phase compositions were identified using a D/max 2550vb+18 kW rotating target X-ray diffraction analyzer (XRD, Rigaku Co.). The scanning angle was in the range of 10°−90° and the scanning speed was 5 (°)/min.

3 Results and discussion

3.1 Effects of infiltrant laying method on microstructure

3.1.1 Cross-sectional morphology

The cross-sectional morphologies of the Zr-based ultra-high-temperature composites are shown in Fig. 1, where Samples P6 and PT6 exhibit dense structures. The cross-section is divided into three

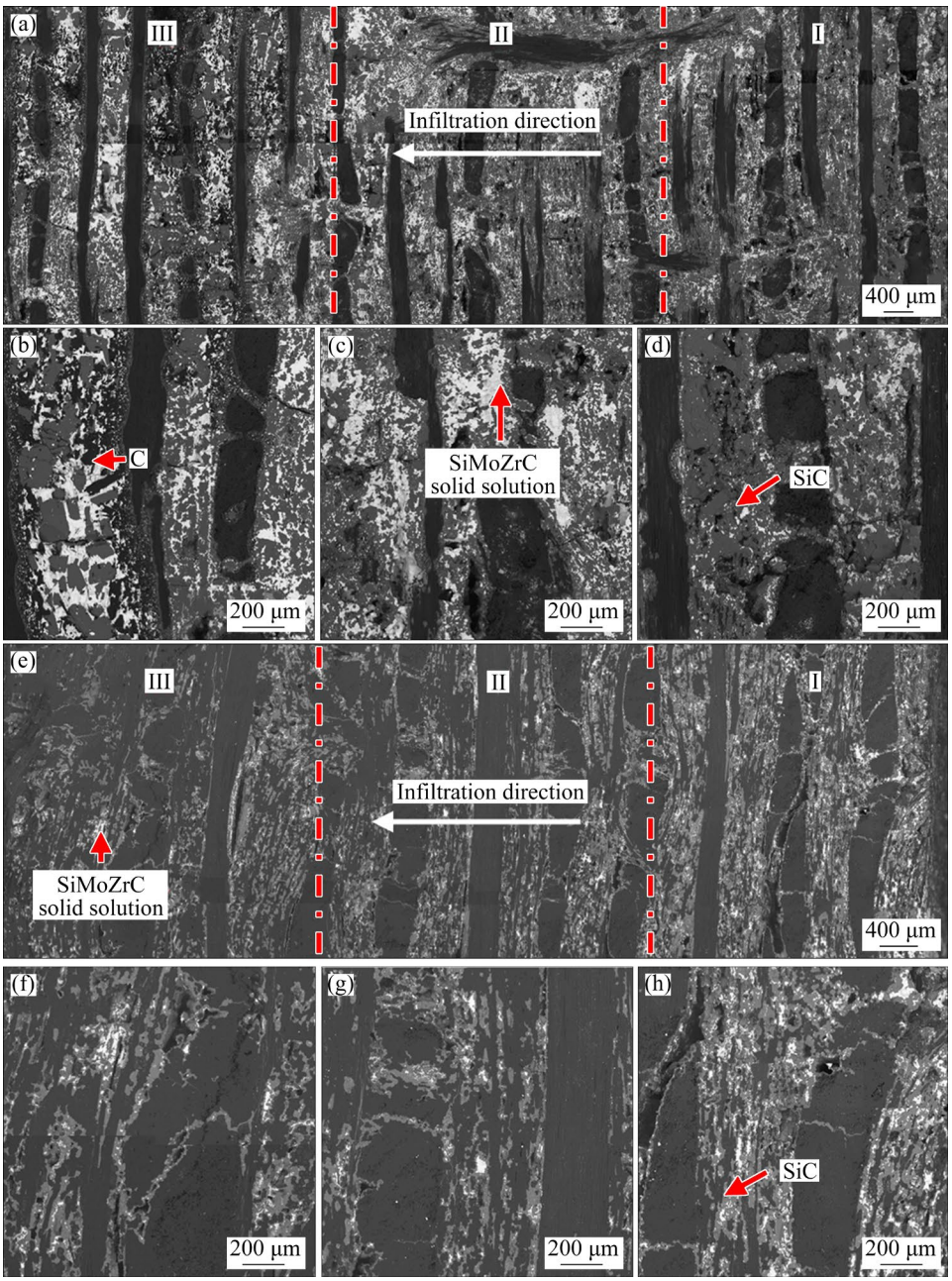

Fig. 1 Cross-sectional morphology of Samples P6 and PT6: (a) P6; (b) Area III of Sample P6; (c) Area II of Sample P6; (d) Area I of Sample P6; (e) PT6; (f) Area III of Sample PT6; (g) Area II of Sample PT6; (h) Area I of Sample PT6

areas: I, II and III. Area I is located close to the infiltrant. Figure 1(a) shows the cross section of Sample P6, which is mainly composed of three phases: black, gray and white, which are identified as C, SiC and SiMoZrC solid solutions, respectively, through energy dispersive spectroscopy. It can be seen that the SiC phase and SiMoZrC solid solution contents decrease and increase gradually along the infiltration direction, respectively. A comparison of Figs. 1(b−d) reveals a change in the ceramic distribution of Sample P6. Figure 1(e) shows the cross-sectional morphology of Sample PT6. As show in Fig. 1(e), the SiMoZrC solid solution content shows no noticeable changes along the infiltration direction. A comparison of Figs. 1(f−h) reveals that the ceramic content in Sample PT6 gradually decreases along the infiltration direction. A comparison of Samples P6 and PT6 shows that the ceramic phase composition changes after infiltration is altered. The SiC ceramic content in Sample PT6 is higher than that in Sample P6, whereas the SiMoSiC solid solution content in Sample PT6 is lower than that in Sample P6. Figures 2(a, b) show cross-sectional morphologies of Samples P8 and P10, respectively. Figure 2(a) shows that the SiMoZrC solid solution content gradually decreases along the infiltration direction; however, the number of pores increases, with the pores being unfavorable for ablation resistance. The ceramic phases of Sample P10 are primarily ZrC and SiC, and the ceramic phase content of the sample exhibits no noticeable changes along the infiltration direction.

To effectively demonstrate the change in the phase content of Zr-based ultra-high-temperature composites, Image-Pro Plus was used, which can make a rough calculation of the ceramic content in the cross section. Figure 3 shows the analytical result, which reveals the distinct variation tendencies of ceramic content along the infiltration direction. The figure shows that the content of the SiMoZrC solid solution in Sample P6 increases along the infiltration direction, which is consistent with the previous analytical results. This indicates that Sample P6 is a gradient material. For Sample P6, the thickness of the Mo layer of the infiltrant is the highest among all the samples, and the resistance of the Mo layer to melt flow is more distinct. This means that Si melts to a greater extent at the early stage, and therefore more SiC and less SiMoZrC solid solution are present in Area I. In Sample P8, the SiMoZrC solid solution and SiC decrease along the infiltration direction. This is because the thickness of the Mo layer of the infiltrant of Sample P8 is smaller, and the resistance of the Mo layer to melt flow is low. Therefore, more melts enter the pores of the C/C composite in the early stage, thus sealing the pores and obstructing melt infiltration. In Sample P10, Si and Zr form a Si−Zr alloy melt favorably and without hindrance from the Mo layer, thus forming a homogeneous

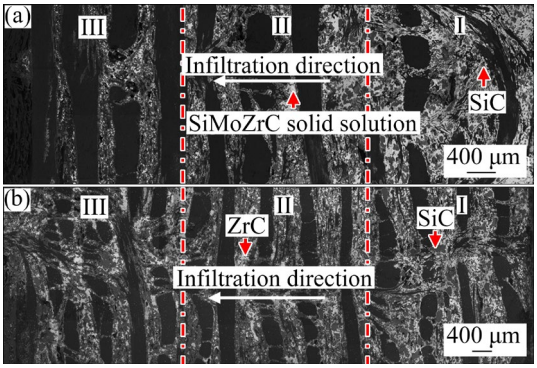

Fig. 2 Cross-sectional morphology of Samples P8 (a) and P10 (b)

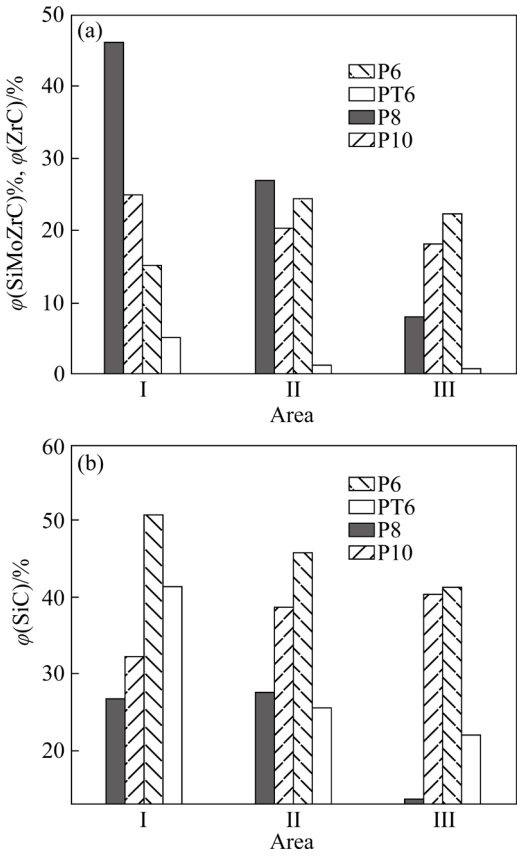

Fig. 3 Volume fraction of ceramic phase: (a) SiMoZrC and ZrC; (b) SiC

composite material. As shown in Fig. 2, the change of the ceramic content is not apparent along the infiltration direction. In Sample PT6, the content of the SiMoZrC solid solution in the sample is minute; however, the SiC content is extensive. This is because the density of the Mo layer in the sample is high. This prevents the Zr and Si melts from mixing. Therefore, only the Si melt infiltrates into the pores at the early stage of infiltration.

3.1.2 Phase composition

To analyze the phase composition of the material, the infiltration surface (Area I) of the gradient material was analyzed by XRD, and the results are shown in Fig. 4. It can be seen that the sample surface consists of C, SiC, $MoSi_2$, ZrC and SiMoZrC solid solutions. Samples P6 and PT6 exhibit the highest SiC diffraction peak, indicating that the SiC content on the infiltration surface is the highest. By contrast, Sample P8 exhibits the highest diffraction peak for the SiMoZrC solid solution, indicating that the content of the solid solution on the infiltration surface is the highest. This result is consistent with the data presented in Fig. 3. A comparison of the XRD patterns of Samples PT6 and P6 reveals that the relative content of the ceramic phase changes significantly when the state of the infiltrating is altered.

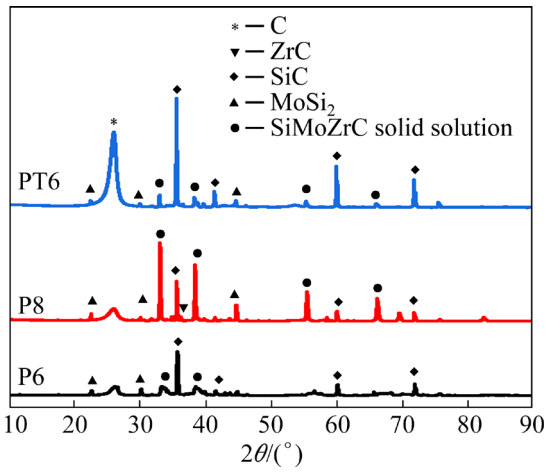

Fig. 4 XRD patterns of gradient material surface

3.1.3 Interface characteristics of carbon−ceramic

To better understand the infiltration mechanism of gradient Zr-based ultra-high-temperature composites, the carbon−ceramic interface was analyzed in this study. According to the distribution and content of the ceramic phase at the interface, the carbon−ceramic interface is divided into three types: SiMoZrC solid solution and C mixture (α-type), continuous SiC ceramics (β-type), and SiMoZrC solid solution and SiC ceramics (γ-type). Figures 5(a−c) show that the carbon−ceramic interfaces of Sample P6 exhibit no distinct changes along the infiltration direction, and all are α-type interface. The SiMoZrC solid solution and C mixture, SiMoZrC solid solution alone, and SiC mixed ceramics comprise the interface components from the carbon fiber to the pore center. This represents the generation sequence of the ceramic phase during the reaction infiltration process. As shown in Figs. 5(d−f), the ceramic distribution at the carbon−ceramic interface changes significantly during infiltration. The carbon−ceramic interfaces in Areas I−III are a continuous SiC ceramic (γ-type), mixture of the SiMoZrC solid solution and SiC ceramic (γ-type), and mixture of the SiMoZrC solid solution and C (α-type). The SiC ceramic is the most abundant in Area I, SiMoZrC solid solution and SiC formed simultaneously in Area II, and SiMoZrC solid solution formed in Area III. A comparison of Figs. 5(g, h) reveals that the carbon−ceramic interface of Sample PT6 is mainly composed of SiC ceramics (β-type). The surrounding carbon fiber is SiC ceramic, indicating that the SiC ceramic forms first. The formation of β-type interface in Sample PT6 is related to the state of the infiltrant. Because the porosity of the infiltrant is low, it is difficult for Mo to dissolve in the Si melt, and the dissolution rate of the infiltrant is slow. Therefore, a large amount of Si melt infiltrates the C/C composites and forms SiC ceramics.

3.2 Infiltration mechanism

Because of the different states and ratios of the infiltrants, the formation process of the melt and the reaction process between the melt and the matrix are different. In addition, the ceramic phase content and distribution of the Zr-based ultra-high-temperature composites are different. This is because the porosities of the various infiltrants are different, which leads to different reaction melt−infiltration processes. Both the distance between the powder particles in the powder-spreading samples and their porosity are large. Owing to the growth of powder particles during the sintering process, the porosity of the pretreated samples is low.

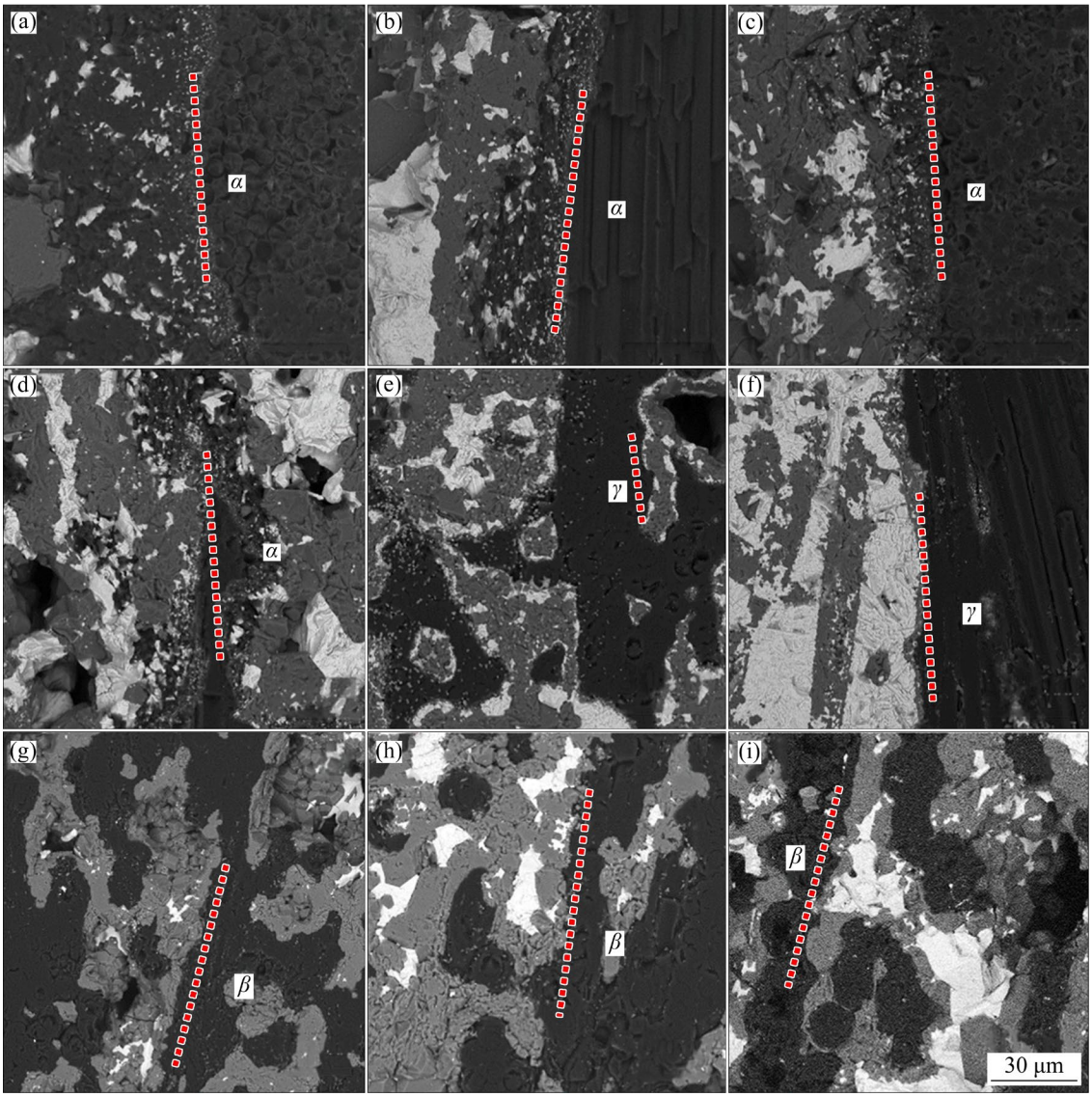

Fig. 5 Morphology of carbon ceramic interface: (a) Area III in Fig. 1(a); (b) Area II in Fig. 1(a); (c) Area I in Fig. 1(a); (d) Area III in Fig. 2(a); (e) Area II in Fig. 2(a); (f) Area I in Fig. 2(a); (g) Area III in Fig. 1(e); (h) Area II in Fig. 1(e); (i) Area I in Fig. 1(e)

Figure 6 shows the infiltration processes with different laying methods. The infiltration processes have two major stages: melting points of Si (1400 °C) and Zr (1850 °C). In Sample P6, the infiltrant contains the Mo layer. When the temperature reaches the melting point of Si, the melting rate of the Si layer is high because the infiltrant is in a powdered state, and the surface energy is also high. Therefore, only the Si melt is present during the initial stage of infiltration. At this stage, under the action of capillary force and gravity, the Si melt gradually penetrates the pores of the C/C composites and Mo layer, which yields Eqs. (3)−(5). However, the Gibbs free energies of $MoSi_2$ and Mo_5Si_3 with C (Eqs. (6) and (7)) are high, rendering the reaction difficult (Fig. 7). When the temperature reaches 1850 °C, Zr begins to melt. In contrast, the Mo layer does not melt at this point, which slows down the infiltration rate of Zr melt into the pores of the sample (Eq. (8)). It leads to the initial penetration of the Si melt into the pores of the sample. As the infiltration progresses, Zr and Mo infiltrated the pores of the material with the Si melt. Therefore, more SiC is present near the infiltrant. For Sample P8, the infiltration process is similar to that of Sample P6. However, the Mo layer of Sample P8 is thin, resulting in more Zr in the Si melt during the early stage (Eqs. (9) and (10)),

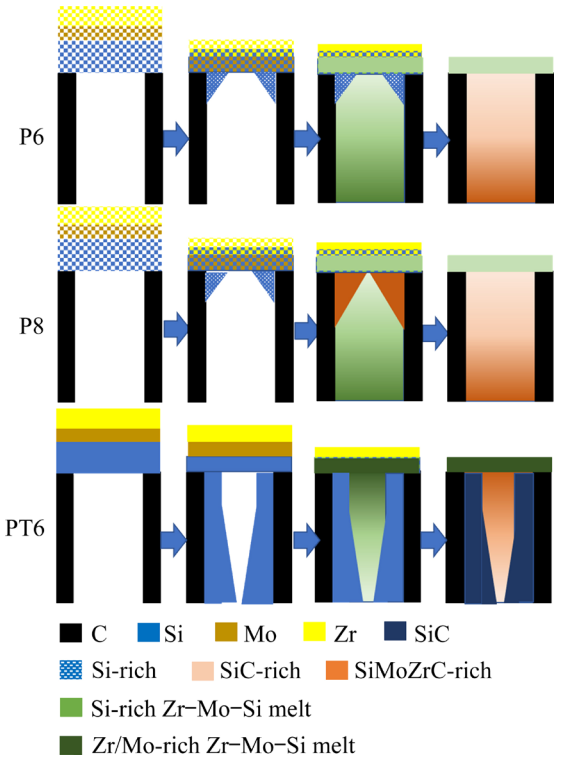

Fig. 6 Schematic diagrams of infiltration process with different laying methods

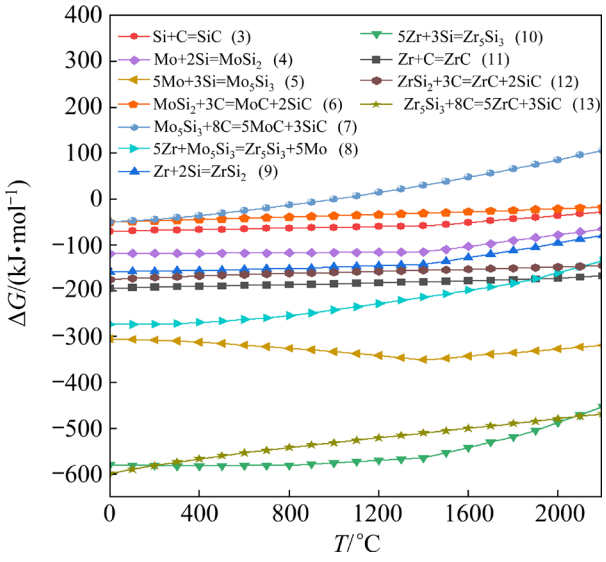

Fig. 7 Gibbs free energy change of main reaction in RMI process

which enters the pores. Because Zr reacts with C more readily, more ZrC is present around the carbon fibers (Eq. (11)). Simultaneously, the ZrC seals the pores, making it difficult for the melt to infiltrate, which leads to a gradual decrease in the ceramic phase content of the sample along the infiltration direction. For Sample P10, the infiltrant contains only the Si and Zr, forming a stable Zr–Si melt. The relative composition of the Zr–Si melt does not change along the direction of infiltration, and a homogeneous material is formed (Eqs. (12) and (13)). For Sample PT6, when Si begins to melt, it is difficult for the Si melt to enter the Mo layer because the porosity of the Mo layer is very low, which results in only a small amount of Mo melting into the Si melt. Simultaneously, the Mo layer hinders the reaction between the Zr and Si melt. Consequently, in the early stage of infiltration, only the Si melt enters the pores of the C/C material and reacts with the pyrolytic carbon. When the temperature reaches 1800 °C, Zr layer begins to melt; however, it is difficult for Zr to penetrate the material owing to the obstruction of the Mo layer. Therefore, only a few Zr and Mo particles infiltrate the pores in the material.

$$Si+C=SiC \quad (3)$$

$$Mo+2Si=MoSi_2 \quad (4)$$

$$5Mo+3Si=Mo5Si_3 \quad (5)$$

$$MoSi_2+3C=MoC+2SiC \quad (6)$$

$$Mo_5Si_3+8C=5MoC+3SiC \quad (7)$$

$$5Zr+Mo_5Si_3=Zr_5Si_3+5Mo \quad (8)$$

$$Zr+2Si=ZrSi_2 \quad (9)$$

$$5Zr+3Si=Zr_5Si_3 \quad (10)$$

$$Zr+C=ZrC \quad (11)$$

$$ZrSi_2+3C=ZrC+2SiC \quad (12)$$

$$Zr_5Si_3+8C=5ZrC+3SiC \quad (13)$$

3.3 Ablative properties and mechanism of gradient Zr-based ultra-high-temperature composites

3.3.1 Ablative properties

The ablation results of the cross-sections of the Zr-based ultra-high-temperature composites exposed to high temperatures for 40 s are shown in Figs. 8 and 9. Figure 8 shows the macroscopic ablation surfaces of the samples, revealing no distinct ablation pits on the surface of Sample P6. However, an oxide film is observed on the surface of Sample P6. Distinct ablation pits are observed on the surfaces of Samples P8 and PT6. Figure 9 shows the mass and linear ablation rates of the samples. The linear and mass ablation rates of Sample P6 are the lowest, and the linear and mass ablation rates of Sample P8 are the highest. In summary, Sample P6 exhibits the highest ablation resistance. To determine the reason of high ablation

resistance for Sample P6, the micromorphology of its ablation cross section was analyzed.

The surface morphologies of the ablated samples are shown in Fig. 10. As shown in Fig. 10(a), the surface of the ablated central area of

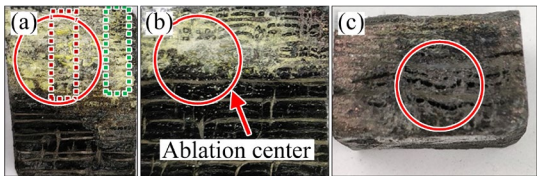

Fig. 8 Macroscopic surfaces of ablated samples: (a) P6; (b) P8; (c) PT6

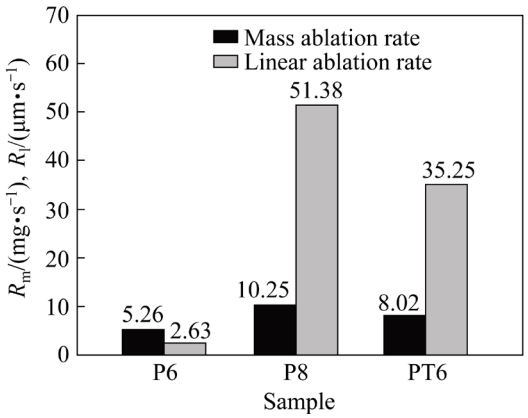

Fig. 9 Mass and linear ablation rates of samples

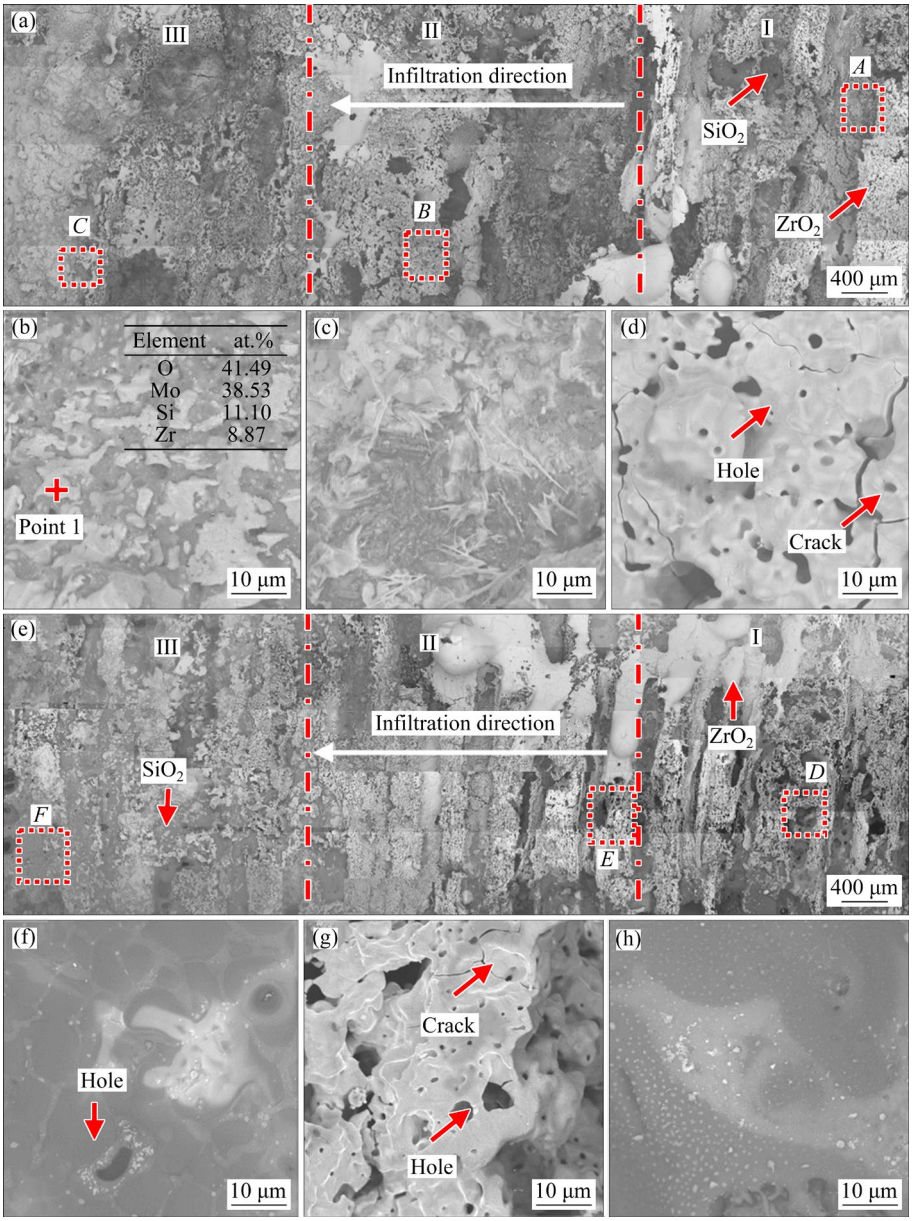

Fig. 10 Morphology of ablated surface of Sample P6: (a) Ablation center area (red rectangular area in Fig. 8(a)); (b) Area *C*; (c) Area *B*; (d) Area *A*; (e) Ablation edge area (green rectangular area in Fig. 8(a)); (f) Area *F*; (g) Area *E*; (h) Area *D*

Sample P6 is a loose ZrO_2 layer. A comparison of Figs. 10(b−d) reveals that the ablated central surface shows no noticeable change along the infiltration direction, and all the ablated samples are composed of loose ZrO_2. Figures 10(b) shows that the surface of the ablation center Area I is mainly ZrO_2, and many pores and cracks are present in the ZrO_2 layer. The pores are caused by the release of gases, such as CO and CO_2, during ablation. Figure 10(c) shows that the surface of Area II is mainly ZrO_2−SiO_2 solid solution, whereas Fig. 8(b) shows that MoO_3 remains on the ablated surface. Figure 10(e) shows that the ablated edge region of the material is mainly composed of ZrO_2, and some molten droplets are present in Areas I and II. The oxide layer in Area III is mainly SiO_2, and the ZrO_2 content on the surface is lower than that in the other areas. The main reason for this phenomenon is that the SiO_2 content in this area is low and cannot fill the pores and cracks in the ZrO_2 layer over time. Therefore, ZrO_2 is removed from the material surface under the action of shear force. As shown in Fig. 10(e), holes caused by the escape of gases, such as CO, CO_2 and MoO_3, appear in the molten droplets. Figure 10(g) shows that many pores and a few cracks are present on the ZrO_2 surface layer. Figures 10(f) and (h) show that the bottom of the ZrO_2 layer is mainly composed of a smooth and flat SiO_2 layer. However, some holes are present in this layer. A comparison of the ablation center area with the ablation edge area reveals that the ablation edge area contains more droplets, and the SiO_2 layer in the ablation edge area is smoother. The ablation center is the closest to the oxyacetylene flame, and the shear and impact forces are the greatest. The droplets flow off the surface of the material under the action of force, whereas the ablation edge is less affected by this force. Therefore, more droplets are present at the edge.

3.3.2 Ablation mechanism

A comprehensive analysis of the ablation center and ablation edge areas shows that the ablation surface morphology of the material varies along the infiltration direction. This is owing to the different contents and distributions of the ceramic phase along the infiltration direction. Area I in Fig. 1(a) has more SiC; however, the content of the SiMoZrC solid solution is relatively low. Therefore, high amounts of SiO_2 and ZrO_2 are produced when the ceramic phase reacts at a high temperature. The viscosity of SiO_2 is low because of the high temperature used in this experiment. Therefore, it easily splashes off the sample surface under the shear force. Because of the low content of ZrO_2, the pinning effect is limited. Finally, the ablated surface of the sample is composed primarily of ZrO_2. In Area II in Fig. 1(a), the SiMoZrC content is higher than that in Area I in Fig. 1(a). However, the content of SiO_2 is relatively low. The ZrO_2 layer on the surface is continuous, indicating the formation of an effective ZrO_2 oxygen barrier layer. In Area III, the sample surface is mainly composed of SiO_2.

4 Conclusions

(1) Zr-based ultra-high-temperature composites were found to be gradient materials when the infiltrant was a powder, and the heights of the two samples of the Zr/Mo/Si layers were 6/4/12 mm and 8/2/12 mm, respectively. However, the ceramic phase varied along the direction of infiltration. The SiMoZrC solid solution content in the first sample increased, whereas that in the second sample decreased.

(2) A comparison of the samples infiltrated by the powder and the prepared tablet infiltrants revealed that altering the state of the infiltrant significantly changed the relative content of the ceramic phase.

(3) An ablation experiment was conducted on the cross sections of the samples, and the anti-ablation results of different ceramic phases were observed under the same conditions. The results showed that the anti-ablation performance of Sample P6 was the best, and the mass and linear ablation rates are 5.26 mg/s and 2.63 μm/s, respectively.

CRediT authorship contribution statement

Qing-hua LIU: Methodology, Formal analysis, Investigation, Data curation, Writing − Original draft; **Tian TIAN:** Methodology, Investigation, Data curation; **Wei SUN:** Project administration, Writing − Review & editing, Funding acquisition; **Hong-bo ZHANG:** Resources, Funding acquisition; **Xiang XIONG:** Resources, Funding acquisition.

Declaration of competing interest

The authors declare that they have no known competing financial interests or personal relationships

that could have appeared to influence the work reported in this paper.

Acknowledgments

This work was supported by the National Natural Science Foundation of China (No. U19A2099), the Open Fund for Hubei Provincial Key Laboratory of Advanced Aerospace Power Technology, China (No. DLJJ2103007), and the Hunan Graduate Research Innovation Project, China (No. CX20220097)

References

[1] BEHRENS B, MÜLLER M. Technologies for thermal protection systems applied on re-usable launcher [J]. Acta Astronautica, 2004, 55: 529−536.

[2] LI Ke-zhi, XIE Jing, LI He-jun, FU Qian-gang. Ablative and mechanical properties of C/C−ZrC composites prepared by precursor infiltration and pyrolysis process [J]. Journal of Materials Science & Technology, 2015, 31: 77−82.

[3] ARAI Y, INOUE R, GOTO K, KOGO Y. Carbon fiber reinforced ultra-high temperature ceramic matrix composites: A review [J]. Ceramics International, 2019, 45: 14481−14489.

[4] WANG Shao-lei, LI Hong, REN Mu-su, ZUO Ya-zhuo, YANG Ming, ZHANG Jia-bao, SUN Jing-liang. Microstructure and ablation mechanism of C/C−ZrC−SiC composites in a plasma flame [J]. Ceramics International, 2017, 43: 10661−10667.

[5] ZHAO Zhi-gang, LI Ke-zhi, KOU Gang, LIU Tian-yu, LI Wei. Mechanical properties and ablation behavior of C/C−ZrC and C/C−ZrC−SiC composites prepared by precursor infiltration and pyrolysis combined with chemical vapor infiltration [J]. Ceramics International, 2018, 44: 23191−23201.

[6] LI Jun, YANG Xin, SU Zhe-an, XUE Liang, ZHONG Ping LI Shuai-peng, HUANG Qi-zhong, LIU Hong-wei. Effect of ZrC−SiC content on microstructure and ablation properties of C/C composites [J]. Transactions of Nonferrous Metals Society of China, 2016, 26: 2653−2664.

[7] LIU Chun-xuan, SU Zhe-an, HUANG Qi-zhong, CHEN Jia-xun, YANG Xin, CAO Liu-xu. YIN Teng, ZHONG Ping. Ablation behavior of ZrC−SiC coated C/C−ZrC−SiC composites prepared by precursor infiltration pyrolysis combined with reactive melt infiltration [J]. Journal of Alloys and Compounds, 2014, 597: 236−242.

[8] ZHAO Zhi-gang, LI Ke-zhi, LIU Qing, ZHANG Yu-lei. Enhanced anti-ablation performance of carbon/carbon composites modified with ZrC−SiC [J]. Vacuum, 2018, 156: 123−127.

[9] TIAN Tian, SUN Wei, QING Xin, XIONG Xiang, ZHANG Hong-bo, CHU Yu-hao, CHEN Zhao-ke, ZENG Yi. Intelligent cooling structure design of “Z-pins like” silicon rods to enhance the ablation resistance of C/C−ZrC−SiC composites above 2500 °C [J]. Journal of the European Ceramic Society, 2020, 40: 3875−3886.

[10] TIAN Tian, SUN Wei, QING Xin, CHU Yu-hao, CHEN Hai-kun, LIU Yu-feng, XIONG Xiang, ZHANG Hong-bo. Effect of surface structure unit of 3D needled carbon fiber preform on the ablation improvement of “Z-pins like” V0.9-Si0.1 rod for C/C−ZrC−SiC [J]. Ceramics International, 2021, 47: 33463−33475.

[11] TIAN Tian, SUN Wei, XIONG Xiang, XU Yong-long, CHEN Yun-tian, ZENG Yi, LIU Fu-qun. Novel “Z-pins like” vanadium rods prepared by solid phase sintering to improve ablation resistance of the C/C−ZrC−SiC composites [J]. Journal of the European Ceramic Society, 2019, 36: 1696−1702.

[12] FENG Wei, ZHANG Yan, LIU Lei, LI Bo-yan, ZHANG Jia-ping, CHEN Xi, HE Zi-bo, TIANG Cheng-wei, ZHANG Hai-jun, HAI Qin-xin. High-frequent pulsing ablation of C/C−SiC−ZrB_2−ZrC composite for different cycles to 2000 times in plasma [J]. Transactions of Nonferrous Metals Society of China, 2023, 33: 553−562.

[13] LIU Tao, NIU Ya-ran, LI Chong, ZHAO Jun, ZHANG Ji-mei, ZENG Yi, ZHENG Xue-bin, DING Chuan-xian. Effect of $MoSi_2$ addition on ablation behavior of ZrC coating Fabricated by vacuum plasma spray [J]. Ceramics International, 2018, 44: 8946−8954.

[14] LIU Tao, NIU Ya-ran, LI Chong, PAN Xiao-hui, SHI Ming-hao, ZHENG Xue-bin, DING Chuan-xian. Ablation resistance of ZrC−$MoSi_2$/ZrC−SiC double-layered coating in a plasma flame [J]. Corrosion Science, 2018, 145: 239−248.

[15] XU Jing-jun, YANG Tian-tian, YANG Yang, QIAN Yu-hai, LI Mei-shuan, YIN Xiao-hui. Ultra-high temperature oxidation behavior of micro-laminated ZrC/$MoSi_2$ coating on C/C composite [J]. Corrosion Science, 2018, 132: 161−169.

[16] HAO Zhen-hua, SUN Wei, XIONG Xiang, XU Yong-long, CHANG Ya-bin, PENG Zheng, CHEN Zhao-ke, WANG Ya-lei. Comparison of microstructure and ablation behavior of Si−Mo−Ti/Al/Zr infiltrated C/C composites prepared at different infiltration temperature [J]. Ceramics International, 2017, 43: 2765−2773.

[17] YAO Dong-jia, LI He-jun, WU Heng, FU Qian-gang, QIANG Xin-fa. Ablation resistance of ZrC/SiC gradient coating for SiC-coated carbon/carbon composites prepared by supersonic plasma spraying [J]. Journal of the European Ceramic Society, 2016, 36: 3739−3746.

[18] HU Cui, NIU Ya-ran, HUANG San-song, LI Hong, REN Mu-su, ZENG Yi, ZHENG Xue-bin, SUN Jin-liang. In-situ fabrication of ZrB_2−SiC/SiC gradient coating on C/C composites [J]. Journal of Alloys and Compounds, 2015, 645: 916−923.

[19] WANG Lu, FU Qian-gang, ZHAO Feng-ling. A novel gradient SiC−ZrB_2−$MoSi_2$ coating for SiC coated C/C composites by supersonic plasma spraying [J]. Surface & Coating Technology, 2020, 313: 63−72.

[20] REN Xuan-ru, LI He-jun, CHU Yan-hui, LI Ke-zhi, FU Qian-gang. ZrB_2−SiC gradient oxidation protective coating for carbon/carbon composites [J]. Ceramics International, 2014, 40: 7171−7176.

[21] REN Xuan-ru, LI He-jun, FU Qian-gang, LI Ke-zhi.

Oxidation protective TaB_2−SiC gradient coating to protect SiC−Si coated carbon/carbon composites against oxidation [J]. Composites (Part B): Engineering, 2014, 66: 174−179.

[22] HE Qin-chuan, LI He-jun, WANG Chang-cong, LI Tao, LU Jin-hua. Microstructure and ablation property of gradient ZrC−SiC modified C/C composites prepared by chemical liquid vapor deposition [J]. Ceramics International, 2019, 45: 13283−13296.

[23] CHANG Ya-bin, SUN Wei, XIONG Xiang, CHEN Zhao-ke, WANG Ya-lei, HAO Zhen-hua, XU Yong-long. Microstructure and ablation behaviors of a novel gradient C/C−ZrC−SiC composite fabricated by an improved reactive melt infiltration [J]. Ceramics International, 2016, 42: 16906−16915.

Zr 基超高温梯度复合材料的显微组织和烧蚀行为

刘清华[1]，田 甜[1]，孙 威[1,2]，张红波[1]，熊 翔[1]

1. 中南大学 粉末冶金国家重点实验室，长沙 410083；
2. 中南大学 轻质高强结构材料国家重点实验室，长沙 410083

摘 要：为了获得高性能 Zr 基超高温复合材料，利用反应熔渗工艺，通过改变原料的铺制方式得到 Zr 基超高温梯度复合材料。研究原料的铺制方式对梯度 Zr 基超高温复合材料显微组织和烧蚀性能的影响。结果表明，当改变熔渗原料的成分比例时，梯度 Zr 基超高温复合材料的梯度结构不同，当 Zr/Mo/Si 层厚度分别为 6/4/12 mm 和 8/2/12 mm 时，样品中 SiMoZrC 固溶体的含量沿着熔渗方向增加和减少。将梯度样品在 3000 ℃的氧乙炔火焰下烧蚀 40 s，当样品的熔渗原料状态为粉末、Zr/Mo/Si 层厚度为 6/4/12 mm 时，材料的抗烧蚀性能最好。

关键词：反应熔渗；陶瓷基复合材料；梯度材料；显微组织；烧蚀性能

(Edited by Xiang-qun LI)